Simultaneous Column-Averaged CO_2, Temperature, and HDO Measurement by Absorption Spectroscopy Lidar: Algorithm

Mingjia Shangguan, Xiaoya Guo, Simin Lin, and Zhongping Lee, *Member, IEEE*

***Abstract*— Carbon dioxide (CO_2) is the most important greenhouse gas in the atmosphere, playing a crucial role in the greenhouse effect and climate change. Lidar, with its high spatiotemporal resolution and high-precision detection capabilities, has become an essential tool for remote sensing of CO_2. However, precise temperature information is required for CO_2 retrieval. Studies showed that for both differential absorption lidar (DIAL) and spectroscopic lidar, a CO_2 concentration measurement error of 2.0–3.5 ppm would result from each 1 K temperature deviation. Therefore, using nonreal-time and non in situ temperature data can lead to significant CO_2 retrieval errors. In this study, a column-averaged CO_2 spectroscopy lidar is proposed, which enables simultaneous measurements of CO_2 concentration, temperature, and semi-heavy water (HDO, isotopic water vapor). First, a model combining five Lorentzian functions with a binomial background was proposed through spectral decomposition. Second, through theoretical analysis, the fitting parameters were reduced from 18 to 5. Finally, theoretical analysis shows that the model achieves system biases of less than 0.1 ppm for CO_2, 0.1 K for temperature, and 0.06 ppm for HDO. Considering Poisson noise, the error distributions of CO_2, temperature, and HDO under different optical distances and signal-to-noise ratios (SNRs) were studied. This technology will advance the development of CO_2 flux remote sensing and is expected to play a crucial role in ecosystem research, atmospheric environmental monitoring, and greenhouse gas emission reduction policies.**

***Index Terms*— Absorption spectroscopy, carbon dioxide (CO_2) measurement, lidar, temperature measurement.**

I. Introduction

IN RECENT years, the increase in atmospheric carbon dioxide concentration (X_{CO_2}) has drawn widespread attention. As of 2023, the global atmospheric average X_{CO_2} has exceeded 420 ppm, a significant rise from the preindustrial level of 280 ppm [1]. Studies have shown that for every 100 ppm increase in X_{CO_2}, the surface temperature of the Earth rises by approximately 1.5 °C [2], [3]. High X_{CO_2} leads to global warming, ocean acidification [4], biodiversity loss, and threats to human health [5]. Therefore, the accurate detection of X_{CO_2} is crucial for understanding and mitigating the impacts of climate change.

Existing in situ measurement techniques, such as high sensitivity cavity ring-down spectroscopy, can achieve remarkable X_{CO_2} measurement precision of 0.1 ppm [6]. However, since these in situ techniques require air sampling, they can only perform fixed-point measurements [6]. In contrast, CO_2 lidar technology enables remote sensing of X_{CO_2} with its high temporal and spatial resolution. Therefore, it is receiving increasing attention and has been applied in volcanic CO_2 flux measurements [7] and urban area CO_2 monitoring [8].

In the past decade, advancements in infrared detection technology and infrared laser technology have significantly improved the performance of CO_2 lidar. To improve detection sensitivity, a CO_2 lidar utilizing a superconducting nanowire single-photon detector (SNSPD) has been developed [9]. Additionally, a 1.57-μm CO_2 lidar based on coherent detection has been designed to simultaneously measure wind speed and X_{CO_2} for flux measurements [10], [11]. To enhance CO_2 detection accuracy and enable the simultaneous measurement of multiple gases, such as H_2O, a multiwavelength lidar system has also been introduced [12], [13]. Furthermore, airborne [14], [15] and spaceborne [16], [17] CO_2 lidars have been proposed to monitor CO_2 uptake over oceans and conduct global CO_2 surveys.

However, whether employing dual-wavelength differential absorption lidar (DIAL) systems or multiwavelength lidar systems, such as spectroscopy lidar systems, converting lidar backscattered signals to X_{CO_2} requires temperature data [18]. In other words, the precision of X_{CO_2} detection is directly influenced by the accuracy of temperature data. However, temperature data are typically obtained from radiosondes or models, which are nonreal time and nonin situ. These temperature data inevitably introduce errors in X_{CO_2} retrieval [19].

Conversely, the sensitivity of CO_2 lidar inversion to temperature implies the potential for simultaneously conducting temperature inversion [12], [13]. Unfortunately, research in this field is relatively limited. On the one hand, the lidar light source must emit enough wavelengths to capture the entire CO_2 absorption spectrum. On the other hand, there is a lack of inversion algorithms capable of simultaneously retrieving both X_{CO_2} and temperature [13], [19].

Meanwhile, once simultaneous measurements of X_{CO_2} and temperature are achievable, it will not only enhance the

Received 30 July 2024; revised 8 November 2024; accepted 26 November 2024. Date of publication 5 December 2024; date of current version 19 December 2024. This work was supported in part by the Innovation Program for Quantum Science and Technology under Grant 2021ZD0303102 and in part by the Fundamental Research Funds for the Central Universities under Grant 20720200107. *(Corresponding author: Mingjia Shangguan.)*

The authors are with the State Key Laboratory of Marine Environmental Science, College of Ocean and Earth Sciences, Xiamen University, Xiamen 361102, China (e-mail: mingjia@xmu.edu.cn; guoxiaoya@stu.xmu.edu.cn; linsimin@stu.xmu.edu.cn; zhongping.lee@umb.edu).

Digital Object Identifier 10.1109/TGRS.2024.3508035

accuracy of lidar measurements of X_{CO_2} but also hold significant importance for calculating CO_2 flux using the eddy covariance method [20]. This is because temperature has a significant impact on turbulent transport processes. Temperature variations can induce buoyancy effects that influence turbulence intensity, which in turn affects the transport and diffusion of CO_2. Additionally, temperature data are crucial for calculating sensible and latent heat fluxes, which help ensure energy balance closure and accurately distinguish the contribution of biological processes to CO_2 flux [21].

In this study, a column-averaged CO_2 spectroscopy lidar is proposed, which enables simultaneous measurements of X_{CO_2}, temperature, and HDO concentration (X_{HDO}). First, the principle of CO_2 lidar is described in detail, and then, the theoretical study of the errors in X_{CO_2} retrieval caused by temperature deviation (ΔT) in both DIAL and spectroscopy lidar is conducted. Then, the feasibility of using the CO_2 absorption spectrum for simultaneous temperature retrieval is validated by analyzing the relationship between temperature parameters and absorption spectrum width. Subsequently, a model for the CO_2 absorption spectrum is proposed, which utilizes a five-peak Lorentzian combined with a binomial background. To improve the fitting efficiency and accuracy, theoretical analysis was conducted to reduce the number of fitting parameters from 18 to only 5. Finally, numerical simulations verify the effectiveness of this algorithm and establish the relationship between the errors in X_{CO_2}, temperature, and X_{HDO} with the signal-to-noise ratio (SNR) and optical distance, thereby providing theoretical guidance for experimental research.

II. Principle of CO_2 Lidar

The backscattered photons received by the CO_2 lidar at a distance of R can be expressed as [22]

$$N_s(x_i, R) = \frac{E \cdot 100}{h \cdot x_i}\eta_0\eta_q \frac{A_t}{R^2} O(R)\frac{\tau}{2}\beta(x_i, R)T_r^2(x_i, R) \quad (1)$$

where N_s is the backscattered photon counts, E is the pulse energy (J), c is the speed of light, x_i is the laser wavenumber (cm^{-1}), R is the distance (m), h is the Planck constant, η_0 is the optical efficiency of the lidar system (%), η_q is the quantum efficiency (%), A_t is the effective area of the telescope (m^2), $O(R)$ is the geometric overlap factor at a distance of R, τ is the laser pulse duration (s), β represents the 180 °C volume backscattering coefficient of aerosols (m^{-1}), and T_r is the transmission term, which can be expressed as

$$T_r(x_i, R) = \exp\left\{-\int_0^R [\alpha_a(x_i, R) + \alpha_s(x_i, R)]dr\right\} \quad (2)$$

where α_a is the extinction coefficient of aerosol (m^{-1}). α_s is the extinction coefficient of molecules and can be described as $\alpha_s = \alpha + \alpha_m$, where α is the absorption coefficient of the gas under investigation and α_m represents other extinction processes of molecules.

The CO_2 lidar measures X_{CO_2} by detecting the absorption of laser signals by CO_2 in the atmosphere. During the measurement process, since wavelength variations are generally within 0.2 pm, β, α_a and α_m can be assumed to be wavelength-insensitive. Hence, the ratio of backscattered photon counts between the two wavenumbers can be expressed as

$$\frac{N_{s_i}}{N_{s_0}} = \exp\left(-2\int_0^R [\alpha_i - \alpha_0]dr\right) \quad (3)$$

where α_i and α_0 are the CO_2 absorption coefficient at the wavenumber of x_i and x_0, respectively.

In the 6360-cm^{-1} spectral interval, with the weak CO_2 absorption line at 6360.60 cm^{-1} serving as a reference point, integrate the absorption coefficient from 0 to R to obtain the optical depth (OD), which is expressed as

$$\mathrm{OD}(x_i, R) = -0.5\ln\left[\frac{N_{s_i}}{N_{s_0}}\right] = \int_0^R [\alpha(x_i, R) - \alpha(x_0, R)]dr. \quad (4)$$

The photon counts $N_s(x_i, R)$ in the 6359.60–6360.60 cm^{-1} band can be reconstructed using (1), resulting in the relative spectra at different distances presented in Fig. 1. Utilizing the data from Fig. 1(a) and applying (4), the OD spectra at different distances can be calculated, as shown in Fig. 1(b). From Fig. 1, it is evident that both the photon count spectra and the OD spectra exhibit increased spectral contrast with increasing distance, which is beneficial for detection.

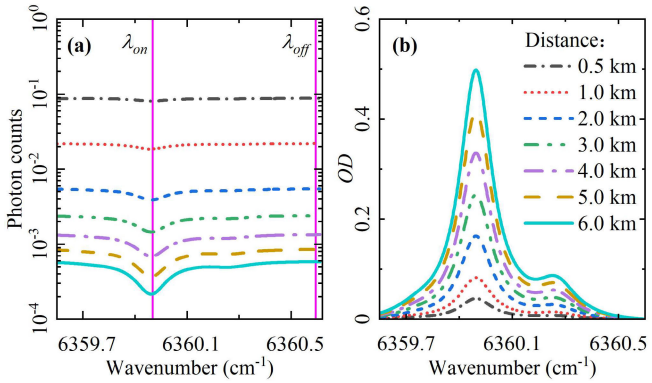

Fig. 1. (a) Spectra of backscattered photon counts $N_s(x_i, R)$ and (b) total OD spectra of CO_2 at various distances under 450-ppm CO_2, 5.28-ppm HDO, 297 K, and 1 atm.

III. Impact of Temperature Deviation on CO_2 Concentration Retrieval

A. Effect of Temperature Deviation on CO_2 DIAL

In CO_2 DIAL, two laser wavelengths are typically used: one located at a strong CO_2 absorption feature, referred to as the online (λ_{on}), and another selected from a weak CO_2 absorption band, known as the offline (λ_{off}). By analyzing the intensity and distance information from the backscattered signal of a hard target, the column-averaged X_{CO_2} can be retrieved [23]. According to (4), the OD of DIAL can be expressed as

$$\mathrm{OD} = -0.5\ln\left[\frac{N_{on}}{N_{off}}\right] \quad (5)$$

where N_{on} is the photon count at λ_{on} and N_{off} is the photon count at λ_{off}. According to OD, the molecular number density of CO_2 N_{CO_2} (molecule/m^3) in the atmosphere can be retrieved as

$$N_{CO_2} = \frac{\mathrm{OD}}{(\sigma_{on} - \sigma_{off})R} \quad (6)$$

where σ_{on} is the absorption cross section of CO_2 at λ_{on} and σ_{off} is the absorption cross section at λ_{off}.

According to the ideal gas state equation, the number density of CO_2 (N_{CO_2}) can be converted to X_{CO_2} [24]

$$X_{CO_2} = \frac{N_{CO_2}}{n} \times 10^6 = \frac{N_{CO_2} k_b T}{P} \times 10^6 \tag{7}$$

where n is the molecular number density of the atmosphere (molecule/m^3), P is the ambient pressure (Pa), T is the ambient temperature (K), and k_b is Boltzmann's constant.

From the above analysis, the impact of temperature deviation ΔT on X_{CO_2} involves two aspects: first, temperature affects the calculation of N_{CO_2} in the process of retrieving X_{CO_2} [as indicated in (7)]; secondly, the CO_2 absorption cross section, which is necessary for calculating N_{CO_2} as described in (6), also depends on temperature data. To simultaneously consider both factors, Han et al. [25] introduced a weighting factor (w) to comprehensively account for the influence, which can be expressed as

$$w = \frac{\sigma_{on} - \sigma_{off}}{k_b T / P}. \tag{8}$$

Thus, (7) can be rewritten as

$$X_{CO_2} = \frac{1}{2wR} \cdot \ln \frac{N_{on}}{N_{off}}. \tag{9}$$

To quantitatively analyze the error of X_{CO_2} (ΔX_{CO_2}) caused by ΔT, this work carried out the following studies: 1) the deviation in the absorption cross section caused by ΔT leads to errors in X_{CO_2}retrieval; 2) when converting N_{CO_2} to X_{CO_2}, as indicated by (7), the impact of ΔT on X_{CO_2} retrieval; and 3) the combined effect of the above two factors on X_{CO_2} retrieval, as shown in (9).

The results from these analyses are shown in Fig. 2. During the simulation process, X_{HDO} was set to 5.28 ppm and pressure to 1 atm. The ΔX_{CO_2} introduced by ΔT when calculating the absorption cross section is shown in Fig. 2(a). That is, assuming there is no temperature deviation when calculating X_{CO_2} using (7), while a temperature deviation is present in calculating N_{CO_2} using (6), resulting in ΔX_{CO_2}. For every 1 K deviation in temperature, the ΔX_{CO_2} increases by 0.68–1.23 ppm. Higher X_{CO_2} and higher temperatures result in larger ΔX_{CO_2}. The ΔX_{CO_2} caused by ΔT when converting N_{CO_2} toX_{CO_2} is shown in Fig. 2(b). That is, assuming there is no temperature deviation when calculating N_{CO_2} using (6), while a temperature deviation is present in calculating X_{CO_2} using (7), resulting in ΔX_{CO_2}. In this case, for every 1 K deviation in temperature, the ΔX_{CO_2} increases by 1.18–2.22 ppm. Furthermore, higher X_{CO_2} and lower temperatures result in larger ΔX_{CO_2}. The combined effect of ΔT on ΔX_{CO_2}, calculated by (9), is shown in Fig. 2(c). That is, assuming temperature deviation exists both in calculating X_{CO_2} using (7) and in calculating N_{CO_2} using (6), resulting in ΔX_{CO_2}. As illustrated in Fig. 2(c), the impact of ΔT on ΔX_{CO_2} varies with different atmospheric temperatures and X_{CO_2} levels. For every 1 K deviation in temperature, ΔX_{CO_2} increases by approximately 1.96–3.28 ppm. Overall, higher X_{CO_2} and lower temperatures lead to larger ΔX_{CO_2}.

TABLE I
PARAMETERS OF THE FIVE ABSORPTION PEAKS USED IN THE MODEL [29]

Formula	$^{12}C^{16}O_2$	$HD^{16}O$	$HD^{16}O$	$^{12}C^{16}O_2$	$^{12}C^{16}O_2$
Peak number	S_1	S_2	S_3	S_4	S_5
AFGL code	626	162	162	626	626
x_0	6359.967	6359.748	6360.278	6360.113	6359.864
$S(T_0)$	1.76×10^{-23}	2.22×10^{-26}	8.62×10^{-26}	3.01×10^{-25}	4.90×10^{-26}
γ_{air}	0.0740	0.0970	0.0954	0.0847	0.0730
γ_{self}	0.100	0.394	0.448	0.116	0.098
E''	106.1297	362.5072	100.3909	675.2049	1521.615
n_{air}	0.70	0.79	0.79	0.69	0.70
P_{self}	-0.00563	-0.00786	-0.01346	-0.00374	-0.00585
abundance	0.984204	0.000311	0.000311	0.984204	0.984204

B. Effect of Temperature Deviation on CO_2 Spectroscopy Lidar

DIAL cannot obtain the full absorption spectrum information of CO_2 because it uses only two wavelengths. To address this limitation, Yu et al. [13] proposed a scheme in 2021 to acquire the CO_2 absorption spectrum, enabling the retrieval of multiple gases, including CO_2 and HDO. To decompose the absorption spectrum CO_2, a model was proposed for nonlinear least squares fitting of the OD spectrum. The model employs three Lorentzian functions, namely, S_1–S_3 (see Table I), to represent the three strongest absorption peaks around 6359.96 cm^{-1}, along with a constant background value (B), which can be expressed as follows:

$$F(x) = f_1(x) + f_2(x) + f_3(x) + B \tag{10}$$

where $f_i(x)$ represents a Lorentzian function, which can be expressed as

$$f_i(x) = \frac{A_i}{\pi} \frac{\omega_{Li}}{\omega_{Li}^2 + (x - x_{ci})^2} (i = 1, 2, 3) \tag{11}$$

where A is the area of the Lorentzian peak (cm^{-2}), ω_L is the half-width at half-maximum (HWHM) of the Lorentzian function (cm^{-1}), and x_c is the central wavenumber of the Lorentzian function under ambient conditions (cm^{-1}).

To obtain distance-resolved OD, the OD is transformed into unit OD (UOD) before performing the fitting as follows:

$$\mathrm{UOD}(x_i, R) = -\frac{1}{2R} \ln\left[\frac{N_{s_i}}{N_{s_0}}\right] = \alpha(x_i, R) - \alpha(x_0, R). \tag{12}$$

In the near-Earth atmospheric environment, the line shape of the absorption peak is the Lorentz line shape [26]. The absorption coefficient at the wavenumber is equal to the sum of the absorption coefficients of all absorption peaks at this wavenumber

$$\alpha(x) = \sum f(x) \tag{13}$$

where $f(x)$ represents a Lorentzian function, as described by (11).

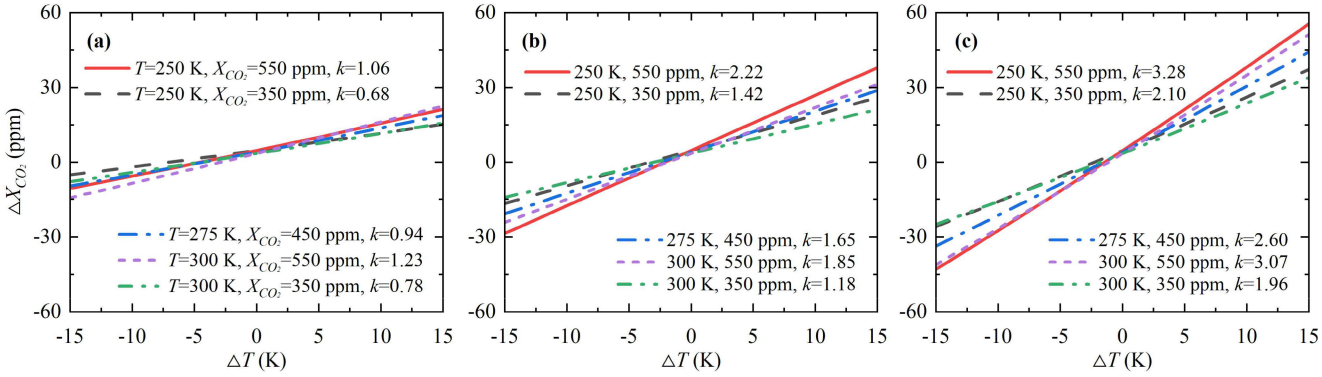

Fig. 2. Analysis of X_{CO_2} retrieval errors (ΔX_{CO_2}) caused by temperature deviation (ΔT) in DIAL. (a) ΔX_{CO_2} resulting from the absorption cross section deviation due to temperature deviation. (b) ΔX_{CO_2} resulting from ΔT when converting N_{CO_2} to X_{CO_2}. (c) ΔX_{CO_2} caused by ΔT under the combined effect of the two factors mentioned above. (The parameter k in the figure represents the slope of the ΔT versus ΔX_{CO_2} curve, indicating the error in ΔX_{CO_2} retrieval for each 1 K deviation).

The area A of the Lorentzian profile is fitted to UOD for the retrieval of CO_2 and HDO concentrations, where A can be expressed as

$$A = \frac{S(T)P_{\text{self}}}{k_{\text{b}}T \times 10^6} \tag{14}$$

where P_{self} represents the partial pressure of the target gas, which can be expressed as

$$P_{\text{self}} = P \cdot X \cdot \text{abundance} \tag{15}$$

where X is the concentration of the target gas, abundance refers to the natural abundance of the target isotope in the environment, and $S(T)$ represents the spectral line intensity at temperature T (cm/molecule), which can be expressed as [27]

$$S(T) = S(T_0)\frac{Q(T_0)}{Q(T)}\left\{\frac{1-\exp(-c_2x_0/T)}{1-\exp(-c_2x_0/T_0)}\right\} \exp\left[E''c_2\left(\frac{1}{T_0}-\frac{1}{T}\right)\right] \tag{16}$$

$$c_2 = \frac{h \times c}{k_{\text{b}}} = 1.4387769\text{cm} \cdot K \tag{17}$$

$$x_c = x_0 + P \times P_{\text{shift}} \times \left(\frac{T_0}{T}\right)^{n_{\text{air}}} \tag{18}$$

where $S(T_0)$ is the spectral line intensity at T_0 (cm/molecule), x_0 is the wavenumber of the spectral line transition (cm^{-1}) in vacuum, $Q(T_0)$ is the total internal partition sum at T_0 and can be downloaded from HITRAN2020, $Q(T)$ is the total internal partition sum at T, c_2 is the second radiation constant, and E is the lower state energy of the transition (cm^{-1}).

Finally, the concentration of the target gas X can be expressed as

$$X = \frac{A}{S(T)n_L}\frac{P_0}{P}\frac{T}{T_0} \tag{19}$$

where P_0 is 1 atm, T_0 is 296 K, and n_L (molecule/m^3) denotes the molecular number density in the atmosphere under the conditions of P_0 and T_0. Additionally, when the concentration of CO_2 is expressed in ppm, the CO_2 concentration needs to be multiplied by 10^6. Similarly, the HDO concentration needs to be multiplied by 10^6 since HDO is expressed in ppm.

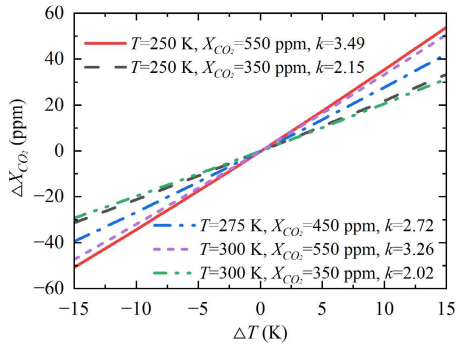

Fig. 3. Effect of temperature deviation on spectroscopy lidar to measure CO_2.

However, it is still necessary to incorporate the temperature information in the retrieval process. The deviation in temperature will lead to errors in the retrieval of X_{CO_2} and X_{HDO}. Assuming other parameters are known and based on the model described in (10), the ΔX_{CO_2} caused by the temperature deviation when using (11)–(19) is shown in Fig. 3. Calculations show that every 1 K deviation in temperature will lead to a 2.02–3.49-ppm deviation in CO_2. However, it is challenging to obtain synchronized and accurate temperature data in experiments. Therefore, obtaining temperature data simultaneously while measuring CO_2 is particularly important.

IV. Feasibility Analysis of Temperature Retrieval via Absorption Spectroscopy

The width ω_L of the absorption spectrum of CO_2 is affected by temperature, and its width can be expressed as [27]

$$\omega_L = \left(\frac{T_0}{T}\right)^{n_{\text{air}}}\left[\gamma_{\text{air}}(P_0,T_0)(P-P_{\text{self}}) + \gamma_{\text{self}}(P_0,T_0)P_{\text{self}}\right] \tag{20}$$

where n_{air} is the coefficient of the temperature dependence of ω_L, P_{shift} is the pressure shift at the spectral line position (cm^{-1}/atm), and γ_{air} and γ_{self} are the air-broadened ω_L (cm^{-1}/atm) and self-broadened ω_L (cm^{-1}/atm) at T_0 and P_0, respectively.

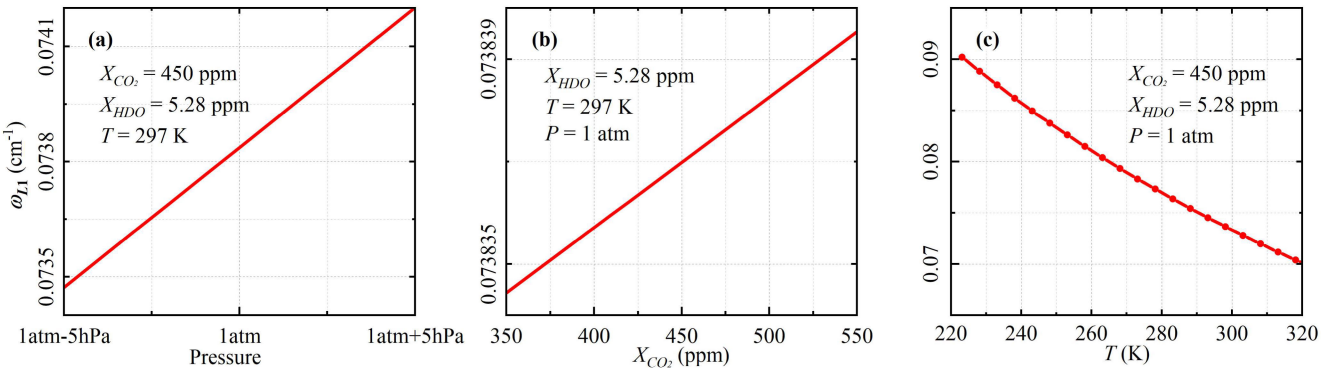

Fig. 4. Effects of (a) pressure, (b) X_{CO_2}, and (c) temperature on ω_L.

As indicated in (20), P, P_{self}, and T codetermine ω_L. The influence of these three parameters on ω_L will be analyzed individually. First, the atmospheric pressure profile is relatively stable in the vertical direction, allowing the use of model data with deviations within ±2 hPa [28]. Fig. 4(a) shows that under 1 atm, variations in ω_L remain within 1% when pressure deviates by ±5 hPa. Therefore, although P influences the magnitude of ω_L, accurate pressure data can minimize the error it introduced. Additionally, the influence of P_{self} on ω_L is approximately in the range of 10^{-5}–10^{-4} of its own magnitude and can therefore be neglected. In (20), $\gamma_{air}(P_0, T_0)(P - P_{self})$ represents the contribution of pressure from other gases in the atmosphere to ω_L broadening, while $\gamma_{air}(P_0, T_0)P_{self}$ represents the contribution of partial pressure from the target gas to ω_L broadening. Fig. 4(b) shows that when X_{CO_2} changes from 350 to 550 ppm at T_0 and P_0, ω_L increased by only 5×10^{-6} cm^{-1}. Additionally, the analysis of ω_L in S_2 revealed that when X_{HDO} increased from 3.11 to 6.21 ppm, ω_L increased by only 9×10^{-7} cm^{-1}, indicating that the magnitude of the variable itself is approximately 10^{-2} cm^{-1}. The above analysis indicates that ω_L is minimally affected by changes in gas concentration.

In contrast, ω_L is much more sensitive to temperature changes than to variations in gas concentration. According to (20), the width of the CO_2 absorption peak S_1, ω_L, can be calculated as the temperature changes from 223 to 324 K. The results are shown in Fig. 4(c), where ω_L changes by approximately 2.5×10^{-4} cm^{-1} for every 1 K change in temperature. This indicates that ω_L is sensitive to temperature variations. In summary, ω_L is minimally affected by gas concentration and is primarily determined by temperature. This provides a basis for using ω_L for temperature retrieval.

However, the three-peak Lorentzian plus background model described by (10) is insufficient for accurately describing CO_2 absorption spectra. As shown in Fig. 5, with X_{CO_2} set to 450 ppm, X_{HDO} set to 5.28 ppm, pressure at 1 atm, and temperature at 297 K, the systematic errors from least-squares fitting using (10) are evident. Fig. 5(a) shows that as X_{CO_2} increases from 350 to 550 ppm, the systematic error of X_{CO_2} rises from 8.5 to 12.7 ppm. Fig. 5(b) indicates that for temperature inversion from 250 to 310 K, the deviation between true and inverted temperatures follows a quadratic function, peaking at 270 K with an error of 4.36 K, decreasing but still above 4.15 K on either side. Fig. 5(c) reveals that the X_{HDO} bias is minimized at 4.66 ppm, increasing on both sides. Thus, to improve accuracy, it is necessary to develop a model that more accurately approximates the real absorption spectrum.

V. Determination of the Absorption Spectrum Model

A. Spectral Decomposition

To accurately describe the absorption spectrum of CO_2, the absorption spectrum needs to be decomposed first. Fig. 6(a) shows the absorption spectrum calculated using data from the HITRAN2020 database [29]. Using the criterion of peak intensities being more than twice as strong as other background absorption peaks, five absorption peaks, labeled S_1 through S_5, are selected, with their locations shown in Fig. 6(a). According to the HITRAN database, the peak positions of these five absorption peaks are 6359.967, 6359.748, 6360.278, 6360.113, and 6359.864 cm^{-1}. In atmospheric CO_2 detection, the influence of atmospheric pressure and temperature on these peak positions is negligible. However, Doppler shifts caused by atmospheric wind speed do affect them. Fortunately, the Doppler-induced frequency shift can be compensated for by adding a wind measurement function to the CO_2 lidar [30]. When the three peaks S_1–S_3, as shown in (10), are subtracted from the spectrum, the resulting spectrum is shown in Fig. 6(b). As shown there, this resulting spectrum cannot be solely represented by the background constant B in (10). This discrepancy is the reason why using (10) to describe the absorption spectrum results in significant systematic deviations in X_{CO_2}, temperature, and X_{HDO}, as shown in Fig. 5.

From Fig. 6(b), it can be observed that peak S_4 has a significant impact on the background. After subtracting S_4, the remaining absorption spectrum is shown as the dashed line in Fig. 6(c), and peak S_5 still stands out in the remaining spectrum. After subtracting S_5, the residual spectrum, shown as the solid line in Fig. 6(c), reveals that the residual background curve can be represented by a binomial. Therefore, to enhance the representation of the absorption spectrum, a model is introduced that describes the CO_2 absorption spectrum using a five-peak Lorentzian combined with a binomial background,

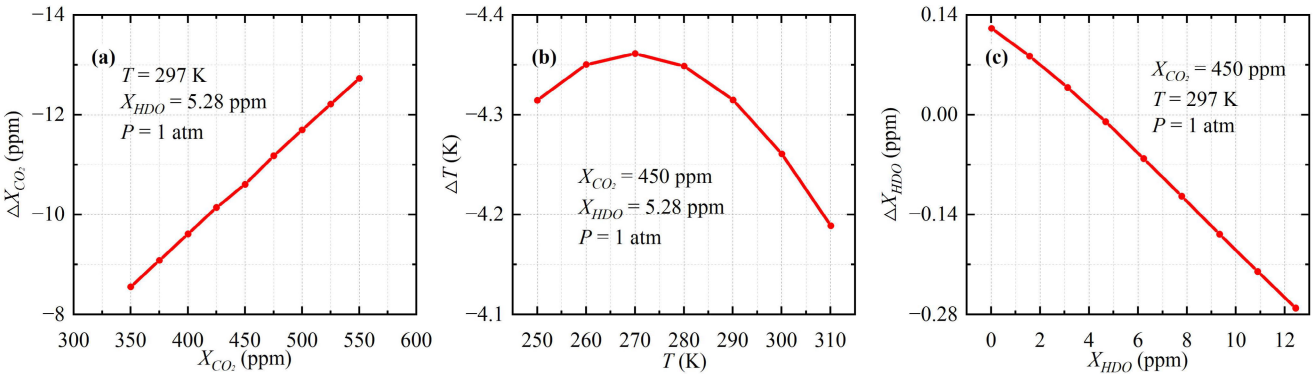

Fig. 5. Systematic errors introduced by the three-peak model described in (10) for (a) CO_2 concentration, (b) temperature, and (c) HDO concentration.

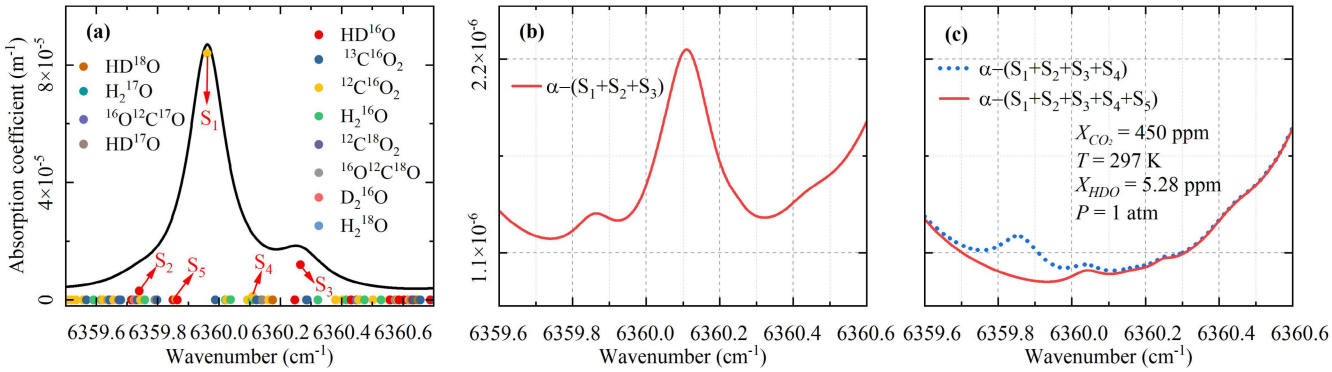

Fig. 6. (a) Absorption spectrum in the 6360-cm^{-1} band. (b) Residual spectrum after removing peaks S_1–S_3. (c) Residual spectrum (solid line) after removing peaks S_1–S_4, and the residual spectrum (dashed line) after removing S_1–S_5.

as shown in the following:

$$F(x) = f_1 + f_2 + f_3 + f_4 + f_5 + a_B(x - b_B)^2 + c_B. \quad (21)$$

The detailed parameters of the five absorption peaks used in the model are listed in Table I.

B. Simplification of Fitting Parameters

However, when the model is updated from three Lorentz functions plus a background, as described in (10), to five Lorentz functions plus a binomial background, as described in (21), the number of unknown parameters to be determined increases to 18. This will significantly increase the difficulty of fitting and reduce its accuracy. Therefore, it is important to find relationships among the parameters in order to reduce the number of variables that need to be decided. First, the central positions of the five Lorentz functions need to be determined. As shown in (18), the central wavenumber is influenced by temperature and pressure. A change of 1 K in temperature results in a change of approximately 1.5×10^{-5} cm^{-1} in the central wavenumber. Similarly, a change of 1 hPa in pressure leads to a change of approximately 5.7×10^{-8}. Therefore, these variations are negligible compared to the central wavenumber itself. Without considering the spectral shift caused by atmospheric wind speed [30], the central wavenumbers of the five Lorentz functions can be treated as known constants, with their specific values presented in Table I. Through the above analysis, the number of fitting 8 to 13. Second, parameter is reduced from 1, as shown in (14), area A is related to gas concentration and spectral line intensity $S(T)$. For the same gas, area A depends solely on the spectral line intensity $S(T)$. According to (16), the ratio between different peaks of the same gas depends only on the parameters of the absorption peaks themselves and the temperature. When the ambient temperature changes, the ratio of each peak area is shown in Fig. 7. For every 1 K increase in temperature, the A_3/A_2 ratio decreases by about 1.67×10^{-3}, the A_4/A_1 ratio increases by about 1.59×10^{-5}, and the A_5/A_1 ratio increases by about 6.40×10^{-6}. Therefore, for the same gas, the area ratios between different peaks can be determined by temperature. In the fitting processes, once the temperature is determined, the ratios of A can be accordingly established. Furthermore, since the ratio of the areas of different peaks for the same gas can be obtained from the temperature, the three unknowns for the CO_2 peak areas, namely, A_1, A_4, and A_5, are simplified to just one. Similarly, the two unknowns for the HDO peak areas, A_2 and A_3, are simplified to one. Moreover, according to the analysis in Section IV, ω_L is mainly affected by temperature rather than gas concentration. Therefore, the ω_L values of the five Lorentz functions can be related through temperature. Calculated according to (20), the ratios of ω_{L2}, ω_{L3}, ω_{L4}, and ω_{L5} to ω_{L1} with respect to temperature are shown in Fig. 8. From the picture, the ratios of each width to ω_{L1} change slightly between 250 and 310 K. For every 1 K increase, the ω_{L2}/ω_{L1} ratio decreases by about 3.97×10^{-4}, the ω_{L3}/ω_{L1} ratio decreases by about 3.90×10^{-4}, the ω_{L4}/ω_{L1}

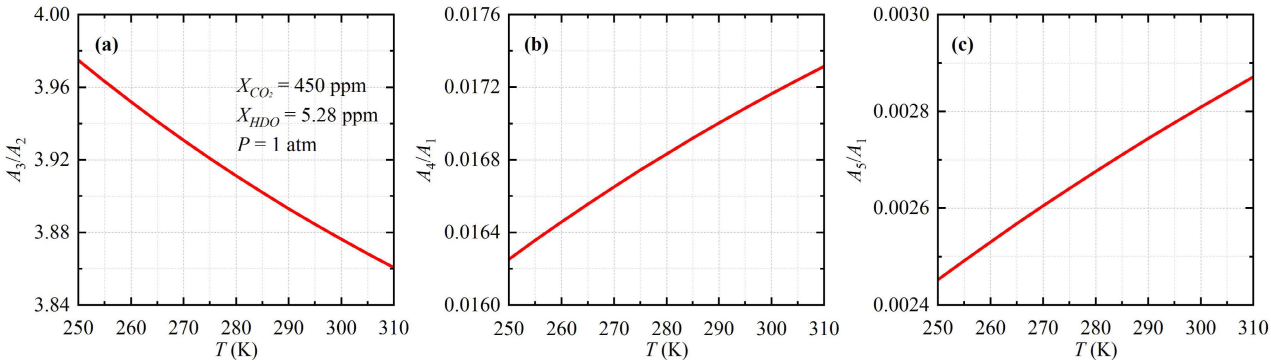

Fig. 7. Effect of temperature on the ratio of the area of absorption peaks (a) S_3 and S_2, A_3/A_2, (b) S_4 and S_1, A_4/A_1, and (c) S_5 and S_1, A_5/A_1.

ratio increases by about 3.85×10^{-5}, and the ω_{L5}/ω_{L1} ratio remains constant at 0.9865. This indicates that the ratios of the widths of the different absorption peaks to ω_{L1} can be considered constants. Therefore, determining ω_{L1} for the CO_2 absorption peak S_1 as the only unknown is sufficient to determine the ω_L values for the other four absorption peaks. Finally, a study on the model background was conducted. By analyzing the residual background spectra after subtracting the absorption spectra of S_1–S_5 under different CO_2 concentrations, HDO concentrations, temperatures, and pressures, it was found that these background values can be accurately fitted using a quadratic equation $a_B(x - b_B)^2 + c_B$. The results are shown in Fig. 9. Fig. 9(a) shows the background spectra for varying CO_2 concentrations. Fig. 9(b) presents the background spectra for different HDO concentrations. Fig. 9(c) illustrates the background spectra under different temperature, and Fig. 9(d) displays the background spectra at various temperatures. As shown in Fig. 9, the background spectra under different conditions can be well fitted using a univariate quadratic equation, with Fig. 9(a) illustrating an example of the fitting results. The analysis of these spectra reveals that the value of b_B consistently regresses to 6359.97, so b_B can be fixed as a constant 6359.97. This analysis reduces the number of unknowns in the background from three to two. Additionally, based on the results from Fig. 9, the initial values for a_B and c_B in the fitting are set to 1.8×10^{-6} and 1.26×10^{-5}. Based on the above analysis, the newly proposed absorption spectrum model, as represented by (21), simplifies the number of unknowns from 18 to 5. These five parameters are the area A_1 of absorption peak S_1, the area A_2 of absorption peak S_2, the ω_{L1} of absorption peak S_1, and the background parameters a and c. Among these, A_1 will be used to retrieve CO_2 concentration X_{CO_2}, A_2 will be used to retrieve HDO concentration X_{HDO}, and ω_{L1} will be used to retrieve temperature.

C. Model Verification

To verify the proposed model (21) and assess the feasibility of the simplified fitting parameters, a simulation and model validation study was carried out. First, the CO_2 absorption spectra in the range of 6359.60–6360.60 cm^{-1} were selected. Thirty wavenumbers were chosen using uniform sampling, with 6360.60 cm^{-1} set as the reference point. The UOD was calculated according to (4) and (12). Subsequently, nonlinear fitting of the UOD was carried out using (10) and (21), respectively. The X_{CO_2} was set at 450 ppm, X_{HDO} at 5.28 ppm, P at 1 atm, and T at 297 K. Initial values for fitting were computed based on these environmental parameters. After the first fitting process was completed, the fitted results were used as initial values for the next fitting until the results of the fitting parameters stabilized. The fitting results of the newly proposed model and the model represented by (10) are shown in Fig. 10. During the computation, the absorption depth was set to 5 km. The analysis of the residuals in Fig. 10(b) and (d) reveals that the newly proposed model performs better, with residuals on the order of $10^{-}8$, which is an order of magnitude lower than those of the model described by (10). Subsequently, similar to Fig. 5, the five-peak model was applied under different environmental parameters to investigate its systematic errors. As shown in Fig. 11, with X_{CO_2} set to 450 ppm, X_{HDO} set to 5.28 ppm, pressure at 1 atm, and temperature at 297 K, the systematic errors from least-squares fitting using (21) are significantly reduced. For X_{CO_2} retrieval, it is found that the systematic errors of the five-peak model are less than 0.1 ppm across the range of X_{CO_2} from 350 to 550 ppm, as shown in Fig. 11(a). Fig. 11(b) shows that for temperature inversion from 250 to 310 K, the temperature deviation is less than 0.11 K, with the minimum error point located at 270 K. For X_{HDO} retrieval, the systematic error increases gradually with the HDO concentration varying from 0 to 12.43 ppm, but the maximum value remains below 0.06 ppm, as shown in Fig. 11(c). These results validate the effectiveness of the new model.

VI. Simulation Analysis

To validate the performance of the new model in a noisy environment, a simulation study was conducted. Since the CO_2 lidar system uses a single-photon detection scheme, its primary noise sources include shot noise (i.e., Poisson noise), solar radiation noise, and detector dark noise. For solar radiation noise, the lidar operates in the near-infrared range, where solar noise is minimal, allowing a narrowband filter to effectively suppress it. Regarding dark noise, current single-photon detection technologies, such as SNSPD, can achieve ultralow system dark count rates [13]. Therefore, this study considers only Poisson noise in the simulation. The specific simulation steps are as follows.

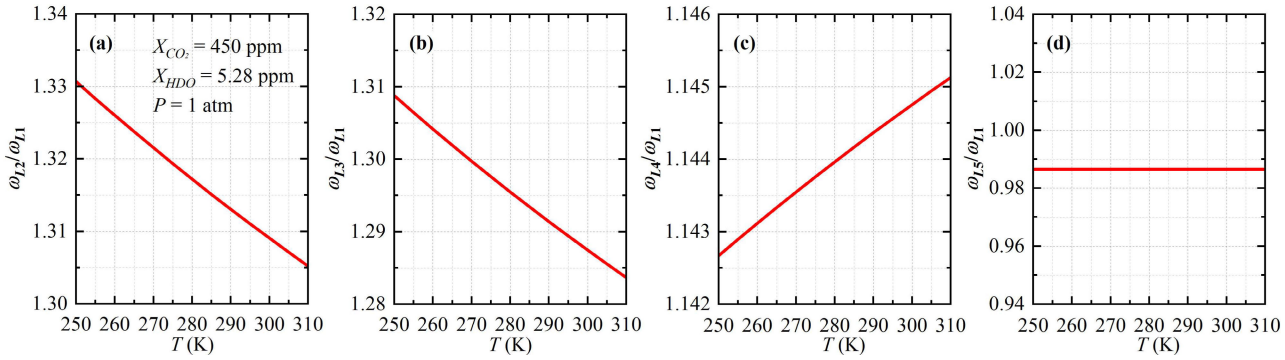

Fig. 8. Effect of temperature on the ratio of ω_L for absorption peaks. (a) S_2 and S_1, (b) S_3 and S_1, (c) S_4 and S_1, and (d) S_5 and S_1.

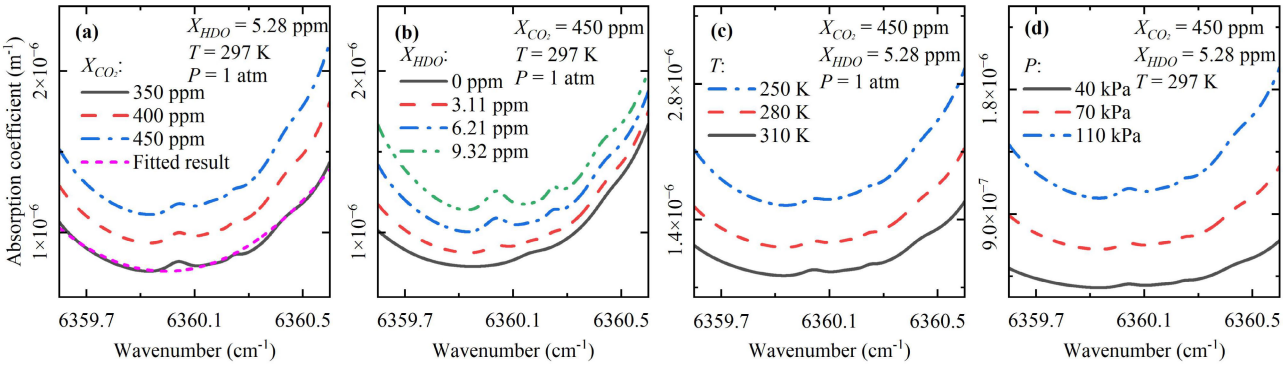

Fig. 9. (a) CO_2 concentration, (b) HDO concentration, (c) temperature, and (d) pressure on the background spectra after removing the five absorption peaks.

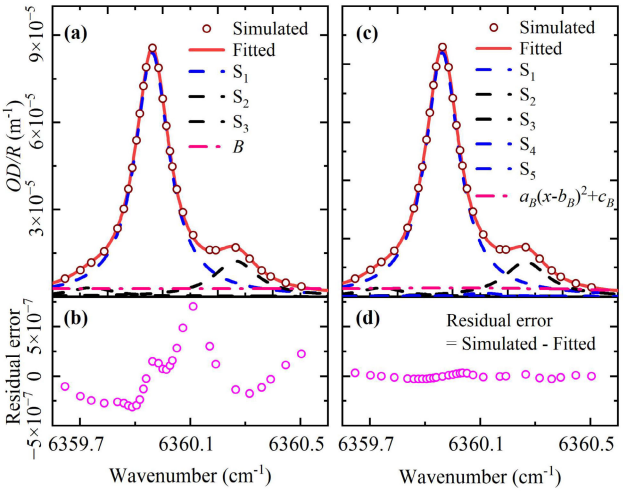

Fig. 10. Fitting results for (a) three-peak model and (c) five-peak model, with corresponding residual error shown in (b) and (d).

Step 1: Calculate the absorption coefficients for 30 wavenumbers uniformly distributed across the spectrum in the range of 6359.60–6360.60 cm^{-1}, based on the atmospheric environment and gas concentrations [13]. During the simulation process, three different environmental conditions were considered: temperature 250 K with a CO_2 concentration of 350 ppm; temperature 297 K with a CO_2 concentration of 450 ppm; and temperature 300 K with a CO_2 concentration of 550 ppm. In all cases, HDO is 5.28 ppm, and P is 1 atm.

Step 2: Simulate the backscattered photon counts at different wavenumbers and distances R using (3), based on specified detection SNR and incorporate Poisson noise into the simulated photon counts. Note that the SNR refers to the SNR at 6360.60 cm^{-1}.

Step 3: Calculate the UOD according to (4) and (12).

Step 4: Perform nonlinear fitting on the simulated UOD using the five-peak Lorentzian model, as described by (21). The initial values of the fitting parameters, A_1, A_2, and ω_L, were calculated based on the following environmental conditions: $X_{\mathrm{CO_2}}$ at 450 ppm, X_{HDO} at 5.28 ppm, P at 1 atm, and T at 297 K.

Step 5: $X_{\mathrm{CO_2}}$, X_{HDO}, and T were calculated using the fitting parameters A_1, A_2, and ω_L, respectively.

Step 6: The initial retrieval results for $X_{\mathrm{CO_2}}$, X_{HDO}, and T calculated in Step 5 are used as the starting values for the next fitting. The iteration stops when the variance of $X_{\mathrm{CO_2}}$ in three consecutive iterations is less than 10^{-9}.

Step 7: Backscattered signal spectra are generated under different SNRs (ranging from 10^2 to 10^4, with intervals of 500) and varying detection distances (ranging from 1 to 10 km, with 1-km intervals). Additionally, Poisson noise is added to each signal spectrum to generate 100 independent sets of data, and Steps 2–6 are repeated to obtain 100 sets of $X_{\mathrm{CO_2}}$, X_{HDO}, and T. Finally, the standard deviation of these 100 sets is then calculated and denoted as$\Delta X_{\mathrm{CO_2}}$, ΔX_{HDO}, and ΔT, respectively.

To obtain analytical expressions for $\Delta X_{\mathrm{CO_2}}$, ΔX_{HDO}, and ΔT with respect to SNR and R, the data underwent the following statistical analysis. Taking the retrieval of$\Delta X_{\mathrm{CO_2}}$

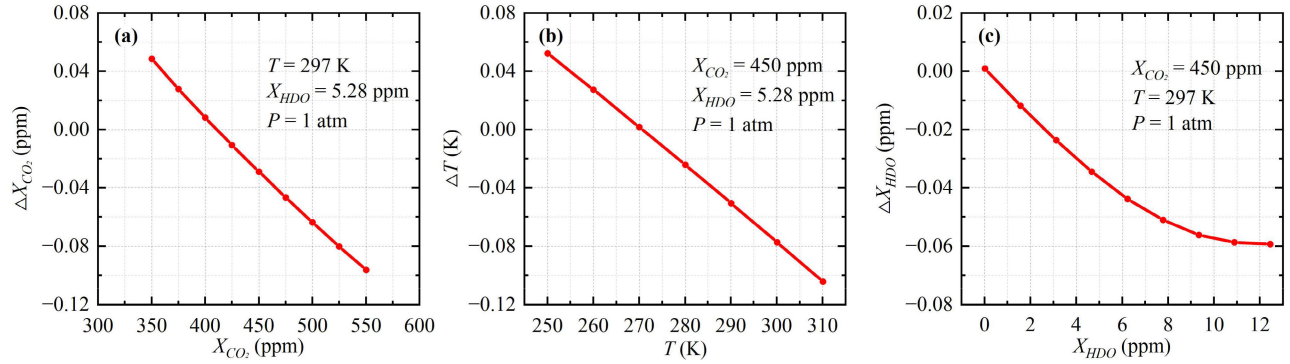

Fig. 11. Systematic errors introduced by the five-peak model described in (21) for (a) CO_2 concentration, (b) temperature, and (c) HDO concentration.

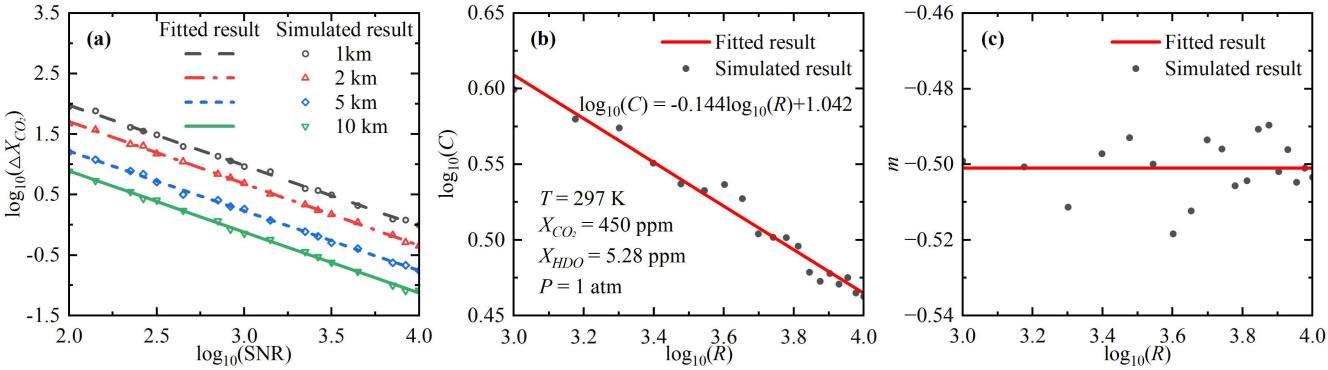

Fig. 12. (a) Relationship between the logarithm of X_{CO_2}, $\log_{10}(\Delta X_{CO_2})$, and the logarithm of SNR, $\log_{10}(\mathrm{SNR})$, at different distances. Dots represent simulation results, while lines show the fitted function $\log_{10}(\Delta X_{CO_2}) = m\ \log_{10}(\mathrm{SNR}) + C$. (b) Relationship between the logarithm of the intercept, $\log_{10}(c)$, and the logarithm of R, $\log_{10}(R)$ and (c) relationship between slope m and the logarithm of R, $\log_{10}(R)$.

under the conditions of a temperature of 297 K and a X_{CO_2} of 450 ppm as an example, the results are shown in Fig. 12(a). As shown in the figure, $\log_{10}(\Delta X_{CO_2})$ decreases monotonically with increasing $\log_{10}(\mathrm{SNR})$ at different detection distances and can be fitted with a linear function: $\log_{10}(\Delta X_{CO_2}) = m\ \log_{10}(\mathrm{SNR}) + C$, where m is the slope of the linear curve and C is the y-intercept. The fitted coefficients of determination (R^2) are all greater than 0.98. The relationship between $\log_{10}(C)$ and $\log_{10}(R)$ is shown by the black data points in Fig. 12(b). This relationship can be fitted as $\log_{10}(C) = -0.144\ \log_{10}(R) + 1.042$, as depicted by the red line in Fig. 12(b). The relationship between m and $\log_{10}(R)$ is shown in Fig. 12(c). Since m only varies slightly, ranging from -0.49 to -0.51, it is taken as the average value of -0.502. Analyzing the above process provides the relationships of ΔX_{CO_2}, ΔX_{HDO}, and ΔT with SNR and R. In the case of a temperature of 250 K and a CO_2 concentration of 350 ppm, the relationships of ΔX_{CO_2}, ΔX_{HDO}, and ΔT with SNR and R can be expressed as

$$\begin{aligned}\Delta X_{CO_2} &= \mathrm{SNR}^{-0.9980} \cdot 10^{R^{-0.1528} \cdot 10^{1.0469}} \\ \Delta T &= \mathrm{SNR}^{-0.9972} \cdot 10^{R^{-0.1727} \cdot 10^{1.0739}} \\ \Delta X_{HDO} &= \mathrm{SNR}^{-0.9994} \cdot 10^{R^{-0.3624} \cdot 10^{1.4728}}.\end{aligned} \tag{22}$$

In the case of a temperature of 297 K and a CO_2 concentration of 450 ppm, the expressions can be updated as follows:

$$\begin{aligned}\Delta X_{CO_2} &= \mathrm{SNR}^{-1.0020} \cdot 10^{R^{-0.1442} \cdot 10^{1.0417}} \\ \Delta T &= \mathrm{SNR}^{-1.0000} \cdot 10^{R^{-0.1676} \cdot 10^{1.0705}} \\ \Delta X_{HDO} &= \mathrm{SNR}^{-1.0076} \cdot 10^{R^{-0.3245} \cdot 10^{1.3730}}.\end{aligned} \tag{23}$$

In the case of a temperature of 300 K and a CO_2 concentration of 550 ppm, the expressions can be updated as follows:

$$\begin{aligned}\Delta X_{CO_2} &= \mathrm{SNR}^{-0.9978} \cdot 10^{R^{-0.1533} \cdot 10^{1.0735}} \\ \Delta T &= \mathrm{SNR}^{-0.9962} \cdot 10^{R^{-0.1838} \cdot 10^{1.1140}} \\ \Delta X_{HDO} &= \mathrm{SNR}^{-0.9968} \cdot 10^{R^{-0.3646} \cdot 10^{1.4984}}.\end{aligned} \tag{24}$$

Under atmospheric pressure conditions at an altitude of 3 km, with P at 70 108 Pa, HDO set to 0 ppm, a temperature of 297 K, and a CO_2 concentration of 450 ppm, the expressions are updated as follows:

$$\begin{aligned}\Delta X_{CO_2} &= \mathrm{SNR}^{-1.0018} \cdot 10^{R^{-0.1419} \cdot 10^{1.0373}} \\ \Delta T &= \mathrm{SNR}^{-1.0018} \cdot 10^{R^{-0.1657} \cdot 10^{1.0623}} \\ \Delta X_{HDO} &= \mathrm{SNR}^{-1.0028} \cdot 10^{R^{-0.3467} \cdot 10^{1.4473}}.\end{aligned} \tag{25}$$

From (22) to (25), it can be observed that the relationships between ΔX_{CO_2}, ΔX_{HDO}, and ΔT with SNR and distance are similar across the three environmental conditions. For instance, with a temperature of 297 K and a CO_2 concentration of 450 ppm, as the SNR increases from 10^2 to 10^4 and R changes from 1 to 10 km, the distributions of ΔX_{CO_2}, ΔX_{HDO}, and ΔT, as described by (19), are illustrated in Fig. 13(a)–(c), respectively. Comparisons between the analytical results and the simulation results are depicted

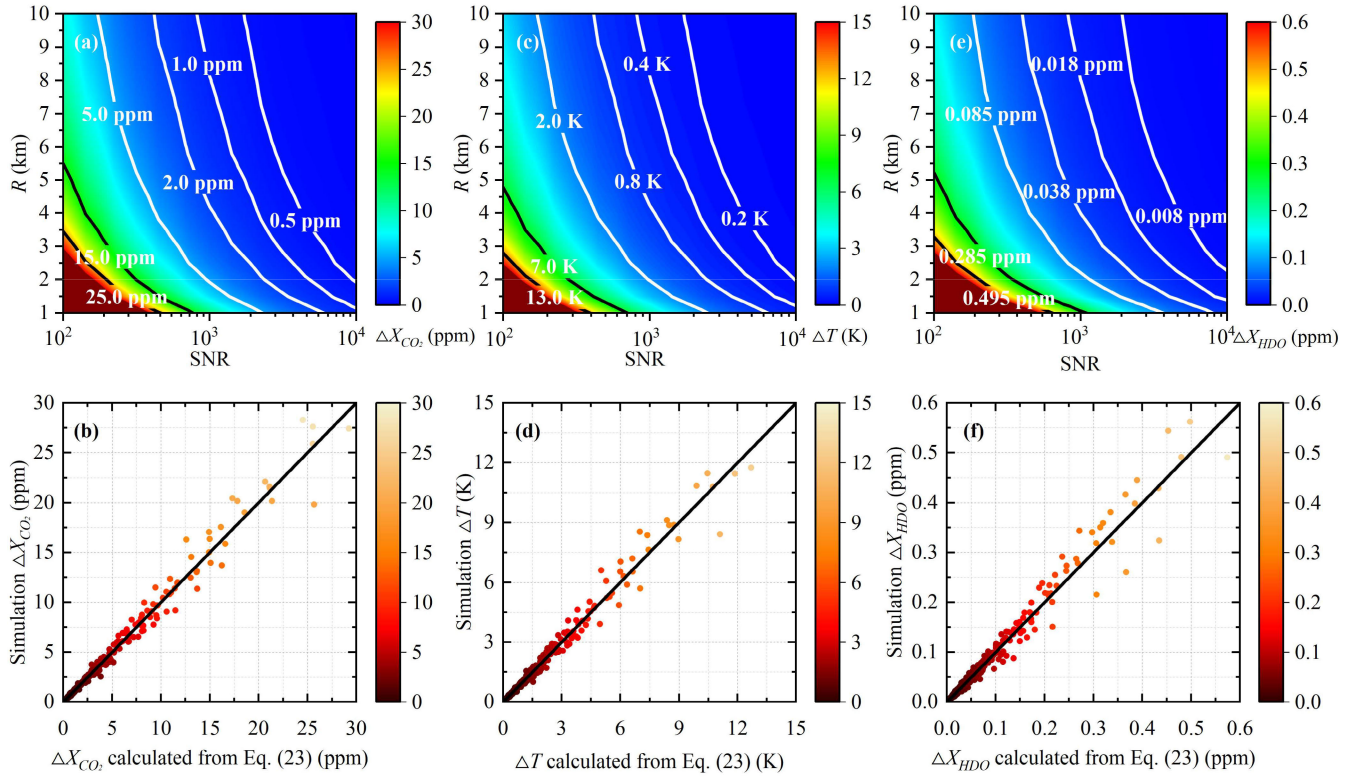

Fig. 13. (a), (c), and (e) Relationship between ΔX_{CO_2}, ΔX_{HDO}, and ΔT with SNR and R, respectively, as described by (23). (b), (d), and (f) Comparison between the analytical results, as described by (23), and the simulation results.

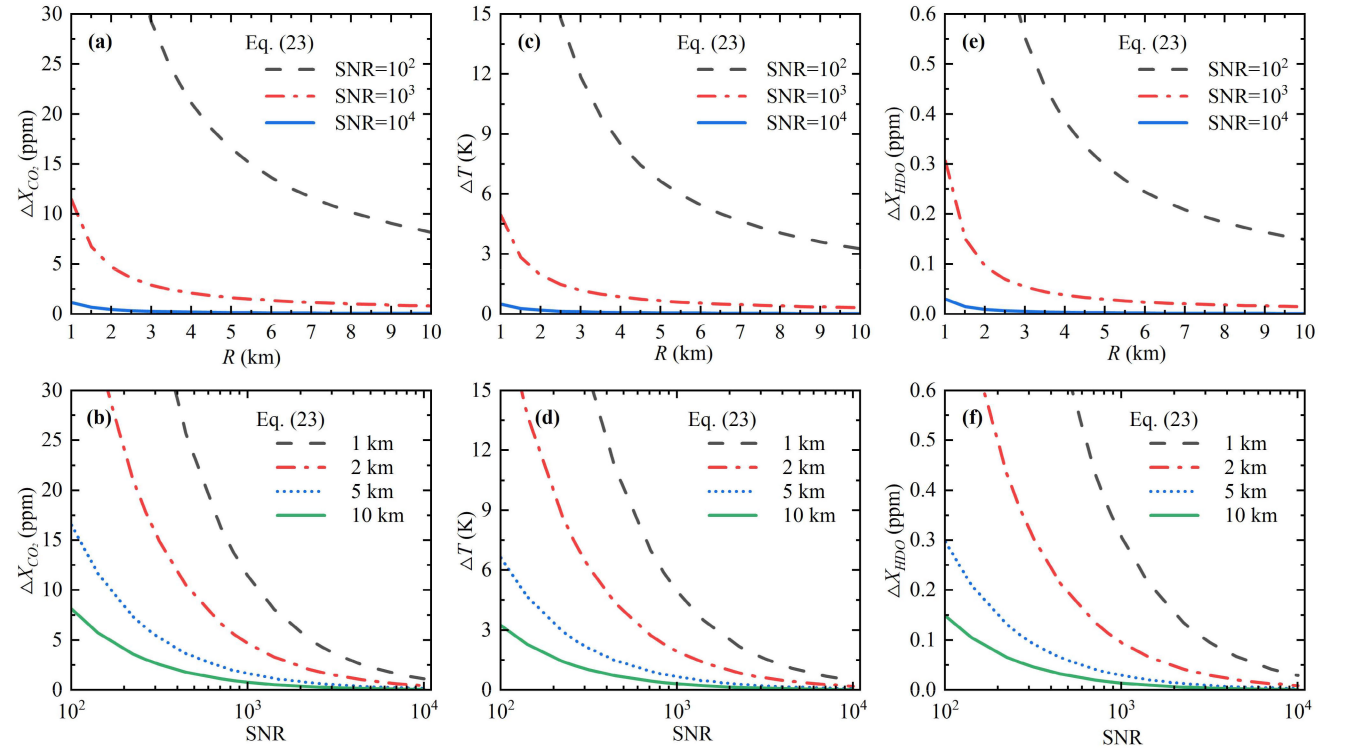

Fig. 14. (a), (c), and (e) Relationship between ΔX_{CO_2}, ΔX_{HDO}, and ΔT with R, calculated using (23), under different SNR levels. (b), (d), and (f) Relationship between ΔX_{CO_2}, ΔX_{HDO}, and ΔT with SNR, calculated using (23), at different R values.

in Fig. 13(d)–(f). These results demonstrate that the analytical expressions provided by (22)–(25) closely match the simulation results for ΔX_{CO_2}, ΔX_{HDO}, and ΔT. This indicates that the equations effectively represent the distributions of

TABLE II
DEFINITIONS AND UNITS OF DIFFERENT SYMBOLS

Parameter	Meaning	Units
N_S	The number of photons returned	
x_i	Wavenumber（The lidar equation, 30 selected points or DIAL selected points）	cm^{-1}
x_c	Central wavenumber of Lorentzian line shape in environmental conditions	cm^{-1}
R	Distance	m
h	Planck's constant	$kg·m^2/s$
k_b	Boltzmann constant	$J·K^{-1}$
T_r	Transmission term	
α	Absorption coefficient of the gas under investigation	m^{-1}
α_i	Absorption coefficient of the gas under investigation at the wavenumber of x_i	m^{-1}
OD	Optical depth	
UOD	Unit optical depth	m^{-1}
N_{CO_2}	Molecular number density of CO_2	molecule $/m^3$
X	Concentration of target gas in the atmosphere	
X_{CO_2}	CO_2 concentration	ppm
X_{HDO}	HDO concentration	ppm
T	Ambient temperature	K
T_0	Standard atmospheric temperature, 296 K	K
P	Ambient pressure	Pa
P_0	Standard atmospheric pressure, 101,325	Pa
w	Weighting function	
k	Fitting slope	
ΔT	Temperature deviation	K
ΔX_{CO_2}	Error between the CO_2 retrieving results and the CO_2 concentration in the environment	ppm
B	Background value of three-peak Lorentz fitting	m^{-1}
A	Area of Lorentzian line shape	
$S(T)$	Spectral line intensity at T	cm/molecule
$S(T_0)$	Spectral line intensity at T_0	cm/molecule
P_{self}	Target gas partial pressure	Pa
$\omega_L(P,T)$	Lorentzian HWHM in environmental conditions	cm^{-1}
n_{air}	Coefficient of the temperature dependence of $\omega_L(P,T)$	
γ_{air}	Air-broadened HWHM at T_0 and P_0	cm^{-1}/atm
γ_{self}	Self-broadened HWHM at T_0 and P_0	cm^{-1}/atm
$Q(T_0)$	Total internal partition sum at T_0	
$Q(T)$	Total internal partition sum at T	
c_2	Second radiation constant	cm·K
x_0	Wavenumber of the spectral line transition in vacuum	cm^{-1}
E''	Lower-state energy	cm^{-1}
P_{shift}	Pressure shift at the spectral line position	cm^{-1}/atm
$abundance$	Abundance of target isotope in nature	

ΔX_{CO_2}, ΔX_{HDO}, and ΔT under varying SNR and distance conditions.

To illustrate these relationships more intuitively, Fig. 14(a)–(c), respectively, shows ΔX_{CO_2}, ΔX_{HDO}, and ΔT variations with the detection range R, at different SNR levels. Additionally, Fig. 14(d)–(f) demonstrates ΔX_{CO_2}, ΔX_{HDO}, and ΔT variations with the SNR at different distances R. From Fig. 14, it can be observed that when the SNR is fixed, ΔX_{CO_2}, ΔX_{HDO}, and ΔT decrease as the distance R increases. Similarly, when R is fixed, ΔX_{CO_2}, ΔX_{HDO}, and ΔT decrease as the SNR increases. From Fig. 14(a), (c), and (e), when the SNR is 10^4, the distance is between 1 and 10 km,ΔX_{CO_2} is less than 1.5 ppm, ΔT is less than 1 K, andΔX_{HDO} is less than 0.04 ppm. For convenience, the definitions and units of the symbols used in this article are listed in Table II.

VII. CONCLUSION

This work proposes an algorithm for simultaneously measuring column-averaged atmospheric CO_2, temperature, and HDO using absorption spectrum lidar, validated through simulations. To reduce system errors, the absorption spectrum was decomposed, and a new model with five Lorentzian peaks and a polynomial background was introduced. The number of fitting parameters was reduced from 18 to 5 through theoretical calculations, significantly decreasing fitted errors. Additionally, simulations established analytical solutions for CO_2, temperature, and HDO under different SNR and detection distances, considering photon counts that follow shot noise (i.e., single-photon detection), thus validating the method's effectiveness. In future work, single-photon CO_2 absorption spectrum lidar experiments will be conducted to validate the practicality of this approach. Furthermore, the measurement capability will be extended from the current column concentrations to distance-resolved measurements. Finally, this technology, combined with wind speed detection capabilities, is expected to be used for eddy covariance measurements of ecosystem CO_2 flux and industrial pollution monitoring applications.

REFERENCES

[1] V. Masson-Delmotte et al., "Contribution of working group I to the sixth assessment report of the intergovernmental panel on climate change," *Climate Change*, vol. 2, no. 1, p. 2391, 2021.
[2] J. Hansen et al., "Climate impact of increasing atmospheric carbon dioxide," *Science*, vol. 213, no. 4511, pp. 957–966, Aug. 1981.

[3] P. M. Cox, R. A. Betts, C. D. Jones, S. A. Spall, and I. J. Totterdell, "Acceleration of global warming due to carbon-cycle feedbacks in a coupled climate model," *Nature*, vol. 408, no. 6809, pp. 184–187, Nov. 2000.

[4] K. Caldeira and M. E. Wickett, "Anthropogenic carbon and ocean pH," *Nature*, vol. 425, no. 6956, p. 365, Sep. 2003.

[5] A. J. McMichael, R. E. Woodruff, and S. Hales, "Climate change and human health: Present and future risks," *Lancet*, vol. 367, no. 9513, pp. 859–869, Mar. 2006.

[6] Y. Lu et al., "Line parameters of the 782 nm band of CO_2," *Astrophys. J.*, vol. 775, no. 1, p. 71, Sep. 2013.

[7] A. Aiuppa et al., "New ground-based LiDAR enables volcanic CO_2 flux measurements," *Sci. Rep.*, vol. 5, no. 1, p. 13614, Sep. 2015.

[8] G. Han et al., "Feasibility study on measuring atmospheric CO_2 in urban areas using spaceborne CO_2-IPDA LiDAR," *Remote Sens.*, vol. 10, no. 7, p. 985, Jun. 2018.

[9] B. Yue et al., "Local-scale horizontal CO_2 flux estimation incorporating differential absorption LiDAR and coherent Doppler wind LiDAR," *Remote Sens.*, vol. 14, no. 20, p. 5150, Oct. 2022.

[10] G. J. Koch et al., "Coherent differential absorption LiDAR measurements of CO_2," *Appl. Opt.*, vol. 43, no. 26, pp. 5092–5099, 2004.

[11] S. Yu et al., "Three-dimensional detection of CO_2 and wind using a 1.57 μM coherent differential absorption LiDAR," *Opt. Exp.*, vol. 32, no. 12, pp. 21134–21148, 2024.

[12] X. Sun et al., "Retrieval algorithm for the column CO_2 mixing ratio from pulsed multi-wavelength LiDAR measurements," *Atmos. Meas. Techn.*, vol. 14, no. 5, pp. 3909–3922, 2021.

[13] S. Yu et al., "Photon-counting distributed free-space spectroscopy," *Light, Sci. Appl.*, vol. 10, no. 1, p. 212, Oct. 2021.

[14] A. Ramanathan et al., "Spectroscopic measurements of a CO_2 absorption line in an open vertical path using an airborne LiDAR," *Appl. Phys. Lett.*, vol. 103, no. 21, pp. 1–4, Nov. 2013.

[15] T. Shi et al., "Quantifying CO_2 uptakes over oceans using LiDAR: A tentative experiment in Bohai bay," *Geophys. Res. Lett.*, vol. 48, no. 9, May 2021, Art. no. e2020GL091160.

[16] C. Fan et al., "Preliminary analysis of global column-averaged CO_2 concentration data from the spaceborne aerosol and carbon dioxide detection LiDAR onboard AEMS," *Opt. Exp.*, vol. 32, no. 12, pp. 21870–21886, 2024.

[17] S. Kawa et al., "Simulation studies for a space-based CO_2 LiDAR mission," *Tellus B, Chem. Phys. Meteorol.*, vol. 62, no. 5, pp. 759–769, 2010.

[18] L. Mei and M. Brydegaard, "Continuous-wave differential absorption LiDAR," *Laser Photon. Rev.*, vol. 9, no. 6, pp. 629–636, Oct. 2015.

[19] C. Xiang, X. Ma, A. Liang, G. Han, W. Gong, and F. Yan, "Feasibility study of multi-wavelength differential absorption LiDAR for CO_2 monitoring," *Atmosphere*, vol. 7, no. 7, p. 89, Jun. 2016.

[20] J. Mayen et al., "Atmospheric CO_2 exchanges measured by eddy covariance over a temperate salt Marsh and influence of environmental controlling factors," *Biogeosciences*, vol. 21, no. 4, pp. 993–1016, Feb. 2024.

[21] G. Burba and D. Anderson, *A Brief Practical Guide to Eddy Covariance Flux Measurements: Principles and Workflow Examples for Scientific and Industrial Applications*. Lincoln, NE, USA: LI-COR Biosciences, 2010.

[22] R. T. H. Collis and P. B. Russell, "LiDAR measurement of particles and gases by elastic backscattering and differential absorption," in *Laser Monitoring of the Atmosphere*, E. D. Hinkley, Ed., Berlin, Germany: Springer, 1976, pp. 71–151.

[23] J. Hamperl et al., "Range-resolved detection of boundary layer stable water vapor isotopologues using a ground-based 1.98μm differential absorption LiDAR," *Opt Exp.*, vol. 30, no. 26, pp. 47199–47215, Dec. 2022.

[24] W. Gong et al., "Sensitivity of on-line wavelength during retrieval of atmospheric CO_2 vertical profile," *Photon. Res.*, vol. 3, no. 4, pp. 146–152, Aug. 2015.

[25] G. Han, W. Gong, H. Lin, X. Ma, and Z. Xiang, "Study on influences of atmospheric factors on vertical CO_2 profile retrieving from ground-based DIAL at 1.6 μm," *IEEE Trans. Geosci. Remote Sens.*, vol. 53, no. 6, pp. 3221–3234, Jun. 2015.

[26] J. Bösenberg, "Differential-absorption LiDAR for water vapor and temperature profiling," in *LiDAR: Range-Resolved Optical Remote Sensing of the Atmosphere*, C. Weitkamp, Ed., New York, NY, USA: Springer, 2005, pp. 213–239.

[27] P. F. Ambrico, A. Amodeo, P. Di Girolamo, and N. Spinelli, "Sensitivity analysis of differential absorption LiDAR measurements in the mid-infrared region," *Appl. Opt.*, vol. 39, no. 36, pp. 6847–6865, Dec. 2000.

[28] B. Zhang et al., "Improving atmospheric pressure vertical correction model using Gaussian function," *Geodesy Geodyn.*, Jun. 2024.

[29] I. E. Gordon et al., "The HITRAN2020 molecular spectroscopic database," *J. Quantum Spectrosc. Radiat. Transf.*, vol. 277, Sep. 2021, Art. no. 107949.

[30] X. Cao et al., "Study on the impact of the Doppler shift for CO_2 LiDAR remote sensing," *Remote Sens.*, vol. 14, no. 18, p. 4620, Sep. 2022.

Mingjia Shangguan received the Ph.D. degree from the University of Science and Technology of China, Hefei, China, in 2017.

He is currently an Associate Professor with the State Key Laboratory of Marine Environmental Science, College of Ocean and Earth Sciences, Xiamen University, Xiamen, China. He has authored or co-authored more than 40 peer-reviewed journal articles and holds 50 Chinese national invention patents and one U.S. patent. His main research interests include single-photon lidar and its applications in marine, atmospheric, and target imaging.

Xiaoya Guo received the B.S. degree from the School of Marine Science and Technology, Tianjin University, Tianjin, China, in 2018. She is currently pursuing the M.S. degree in marine chemistry with Xiamen University, Xiamen, China.

Her research interests include atmospheric monitoring lidar.

Simin Lin received the B.E. degree from the School of Environmental and Safety Engineering, Fuzhou University, Fuzhou, China, in 2019. She is currently pursuing the M.E. degree in environmental engineering with Xiamen University, Xiamen, China.

Her research interests include atmospheric monitoring lidar.

Zhongping Lee (Member, IEEE) received the Ph.D. degree from the University of South Florida, Tampa, FL, USA, in 1994.

He is currently a Professor with the State Key Laboratory of Marine Environmental Science, College of Ocean and Earth Sciences, Xiamen University, Xiamen, China. He has authored or co-authored more than 130 peer-reviewed journal articles. He led the development of the widely used quasi-analytical algorithm (QAA) and the hyperspectral algorithm (HOPE) for processing both optically deep and shallow waters, along with various applications of satellite ocean color products. His main research interests are in optical oceanography and ocean color remote sensing.

Dr. Lee is a fellow of the Optical Society of America. He is a member of many science teams for ocean color remote sensing.